THREE-DIMENSIONAL COMPUTATIONS OF TRANSVERSE HELIUM JETS IN A SUPERSONIC AIR FLOW

P.Y. TZENG AND J.H. SHEU

Department of Aeronautical Engineering, Chung Cheng Institute of Technology, Tahsi, Taoyuan, Taiwan 33509, Republic of China

ABSTRACT

This paper describes a study concerning the numerical simulation of a sonic helium jet through a transverse nozzle in a flat plate exhausting normally into a supersonic air flow. Three-dimensional Reynolds-averaged Navier-Stokes equations coupled with the modified Baldwin-Lomax algebraic turbulence model and relevant species equations are solved by using a finite-volume upwind scheme. In this approach, Roe's flux function, explicit multi-stage integration and multi-block procedure are applied to achieve the steady state solution efficiently. The Roe's flux function is modified to suit the simulation of helium-air mixing. The comparison between two-dimensional calculated results with experimental data of surface pressure shows good agreement. The results of three-dimensional computations for square, circular and rectangular jets are presented, and the essential flow features including induced shocks, upstream separations, and downstream primary and secondary vortices are adequately simulated.

KEY WORDS   Transverse jet   Supersonic flow   Two-species mixing   Finite-volume method

INTRODUCTION

The interactions of single or multiple jets with a free or confined crossflowing mainstream plays a very important role in a wide variety of practical engineering situations. This "jet-in-crossflow" type of flow is especially relevant to the studies of many jet propulsion and reaction control problems. The injection of transverse jets into a supersonic main flow is a frequently utilized technique for flight control of an aerospace vehicle, thrust vector control of rocket motors, and for supersonic combustion in ramjet engines. In particular, for an advanced tactical missile, design of reaction jets as control devices has been suggested to meet the requirements of high manoeuverability and rapid response. One basic situation suitable for numerical investigation on reaction jet effects at supersonic speeds is the sonic injection of gaseous injectant through a nozzle and normal to a supersonic airstream over a flat plate.

The typical features of the interaction flowfield due to a transverse sonic jet in supersonic crossflow can be described by referring to the schematic drawing in *Figure 1*. We consider a two-dimensional jet issuing along y-direction from an injection nozzle in a plane wall into a cross-stream of M_∞ in x-direction. The jet flow is highly underexpanded at the nozzle exit and expands rapidly through strong Prandtl-Mayer fans, then followed by compression to form a Mach disk and bent aft by the main flow. The blockage presented by the jet to the external flow causes a strong bow shock and separates the turbulent boundary layer ahead of the injection point. In the separation region, at least two counter-rotating vortices can be found. A weak separation shock is induced accordingly. In the lee of the jet, another region of separated flow is apparent, and an
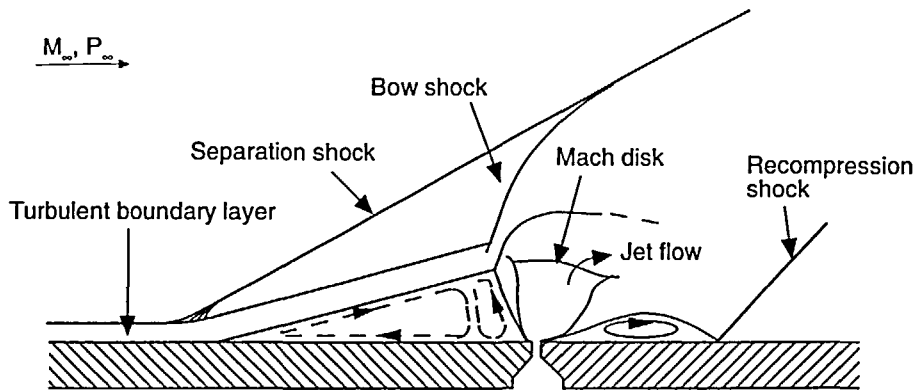
Figure 1a   Schematic diagram of a two-dimensional jet in supersonic crossflow
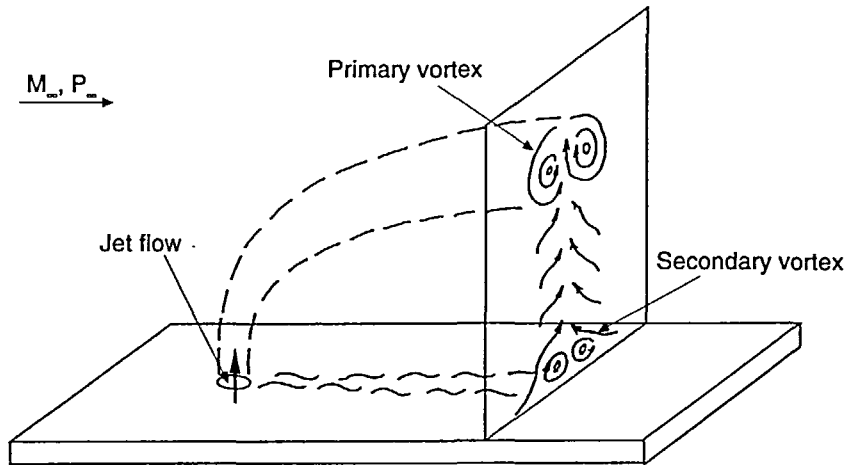

Figure 1b   Three-dimensional vortex structure downstream of the jet

associated recompression shock is formed to turn the flow parallel to the solid wall. The general characteristics of a three-dimensional jet interacting with a supersonic planar flow are similar to those of the two-dimensional case. However, the interaction intensity in the 3-D case is reduced because the flow can go sideways around the jet in addition to going upward over it. One prominent feature of 3-D jet in a crossflow is the presence of a primary vortex pair structure, as shown in *Figure 1(b)*, which is observed to dominate the downstream cross section of the jet. Another smaller secondary vortex pair located beneath the primary vortex and very close to the wall is also observed.

A significant number of experimental and analytic investigations for the jet-in-crossflow interaction were performed during the 1970s. The literature pertaining to the interaction of a sonic or supersonic gaseous jet with a transverse external flow has been reviewed by Werle[1] and Spaid and Cassel[2]. A more recent experimental study has been presented by Aso *et al.*[3] Previous numerical studies of sonic or supersonic jets in a supersonic crossflow were not apparent until 1988 and were presented by Harloff and Lytle[4]. A sonic jet of air with a supersonic crossflow of

Mach number 2.92 was studied. Laminar flow was assumed for the calculations. The surface pressure distribution, except immediately upstream of the nozzle exit, is in reasonable agreement with the test data conducted by Cubbison et al.[5] Thompson[6] adopted a finite volume method to simulate the flowfield of 2-D transverse jet with $M_\infty = 2.61$. The turbulence model used was the two-layer algebraic model of Baldwin and Lomax. The agreement between numerical results and experimental data, presented by Spaid and Zukoski[7], was only fair. The upstream separation and downstream re-attachment were not accurately predicted. It was suggested that the discrepancy may be improved by using an advanced turbulence model and a numerical limiter.

Dormieux et al.[8] presented a numerical study for solving the 3-D Euler equations for a non-reactive mixture of two perfect gases. The Mach number of crossflow is 2, and the Mach number of jet is 2 for air and 2.5 for a helium injectant. The effect of various injectants was studied for a given dynamic pressure at the nozzle exit. Numerical investigations on mixing and combustion of injecting hydrogen jet into supersonic air flow, including nine species and 19 elementary chemical reactions, were presented by Takahashi and Hayashi[9]. They suggested that the wall heat transfer should be taken into consideration to avoid the overestimation of heat deposit from the chemical reaction near the wall. The modified k-ε turbulence model was first considered by Rizzetta[10]. The agreement with experimental data was poor as the width of the nozzle exit increased, this is due to the lack of knowledge of the turbulence properties at the nozzle exit. Details of the comparison of the aforementioned numerical studies are listed in *Table 1*.

In this study, a finite-volume upwind scheme is presented to solve the time-dependent Reynolds-averaged Navier-Stokes equations coupled with the modified Baldwin-Lomax turbulence model[11] and relevant species equations. The solver utilizes a cell-centred, physical space, finite volume, upwind scheme to simulate this complex supersonic interaction flowfield. The semi-discretized unsteady equation is then solved by an optimally smoothing multi-stage scheme[12] integrated with local time stepping[13] and an implicit residual smoothing (IRS)[13] to accelerate the convergence. In order to impose an adequate boundary condition at the nozzle exit, a multi-block alternative iteration procedure is implemented. Some efforts are directed first to the problem of 2-D jet in supersonic crossflow. This serves as a useful test problem for evaluating the effectiveness of computational schemes for the much more complicated 3-D cases. Three-dimensional computations are then made for the jet/external-stream flow of non-reactive helium and air over flat plate. The effect of different shapes of the nozzle exit, square, circular and rectangular, is also investigated.

GOVERNING EQUATIONS

Governing Equations

The integral form of the time-dependent Reynolds-averaged Navier-Stokes equations in a Cartesian system[14], with a species equation, is,

$$\frac{\partial}{\partial t} \iiint_\Omega U d\Omega + \iint_S \Phi \cdot n dS = 0 \tag{1}$$

where t is the time, Ω and S are the volume and surface of control volume, and n is the normal unit vector of the element surface. The column vector U contains the conservative variables and Φ contains the fluxes. The Cartesian components of U and the components F, G, H of the flux vector-tensor Φ are defined as follows:

Table 1 Comparison with the previous numerical investigations of the jet in supersonic crossflow over a flat plate

Year	Authors	Physical model	Mathematical model	Turbulence model	Method	Mesh	Parameters	Injectant
1988	Harloff and Lytle[4]	3-D, circular exit	Novier-Stokes equation		FDM: Implicit beam-warming scheme	$50 \times 31 \times 21$	$M_\infty = 2.92$ $M_j = 1$	air
1989	Thompson[6]	2-D	unsteady RANS equation	Baldwin-Lomax model	FVM: Roe's scheme or osher's scheme Line Gauss-Seidel relaxation scheme	adaptive structure grid 100×60, 150×60	$M_\infty = 2.61$ $M_j = 1$	nitrogen
1990	Dormieux *et al.*[8]	3-D, square exit	Euler equation species equation (2)		FVM: MUSCL approach +Roe's scheme +1st-order time-integration method	$35 \times 40 \times 60$ multi-domain: $45 \times 41 \times 49$ and $23 \times 45 \times 49$	$M_\infty = 2$ $M_j = 2$ for helium $M_j = 2.5$ for air	air helium
1991	Takahashi and Hayashi[9]	2-D	RANS equation species equation (9) chemical reactions (19)	Baldwin-Lomax model	FDM: Implicit Harten-Yee type TVD scheme	97×67 (non-reaction), 67×57 (reacting)	$M_\infty = 1.81$ $M_j = 1$	hydrogen
1992	Rizzetta[10]	2-D	RANS equation	k-e turbulence model	FDM: MacCormark scheme	235×81	$M_\infty = 3.71$ $M_j = 1$	air
1994	Present study	2-D, 3-D, circular, square, rectangular exit	RANS equation +species equation	Baldwin-Lomax model	FVM: van Leer kappa scheme Roe's scheme+ Multi-stage method	Multi-block: 3-D: Rectangular jet: $90 \times 40 \times 35$ and $27 \times 24 \times 18$: Square jet $96 \times 58 \times 40$ and $15 \times 30 \times 15$. Circular jet: $65 \times 45 \times 50$ and $65 \times 30 \times 15$	$M_\infty = 2.61$ $M_j = 1$	helium

Key: RANS:Reynolds-averaged Navier-Stokes equations, FDM: Finite difference method, FVM: Finite volume method

$$
U = \begin{bmatrix} \rho \\ \rho u \\ \rho v \\ \rho w \\ \rho E \\ \rho C_i \end{bmatrix} \quad
F = \begin{bmatrix} \rho u \\ \rho u^2 + p - \tau_{xx} \\ \rho uv - \tau_{xy} \\ \rho uw - \tau_{xz} \\ \rho u H^* - u\tau_{xx} - v\tau_{xy} - w\tau_{xz} + q_x \\ \rho u C_i - \rho D_{ij}\dfrac{\partial C_i}{\partial x} \end{bmatrix}
$$

$$
\text{(2)}
$$

$$
G = \begin{bmatrix} \rho v \\ \rho uv - \tau_{xy} \\ \rho v^2 + p - \tau_{yy} \\ \rho vw - \tau_{yz} \\ \rho v H^* - u\tau_{xy} - v\tau_{yy} - w\tau_{yz} + q_y \\ \rho v C_i - \rho D_{ij}\dfrac{\partial C_i}{\partial y} \end{bmatrix} \quad \text{and } H = \begin{bmatrix} \rho w \\ \rho uw - \tau_{xz} \\ \rho vw - \tau_{yz} \\ \rho w^2 + p - \tau_{zz} \\ \rho w H^* - u\tau_{xz} - v\tau_{yz} - w\tau_{zz} + q_z \\ \rho w C_i - \rho D_{ij}\dfrac{\partial C_i}{\partial z} \end{bmatrix}
$$

where $\rho, u, v, w, p, E, H^*, \tau$ and C_i denote nondimensional density, Cartesian velocity components, pressure, total energy, stagnation enthalpy, shear stresses and mass fraction of species i. D_{ij} is the binary diffusion coefficient obtained from the Fick's rule[15]. For the gas dynamic computation, the concentration gradients induced by the pressure and temperature diffusion can be neglected such that it is dominated by the mass diffusion only. Therefore, the heat fluxes are composed of the heat conduction flux and the transport of enthalpy induced by mass diffusion,

$$
q = -\kappa \nabla T + \sum_i \rho_i V_i h_i = q_x \vec{i} + q_y \vec{j} + q_z \vec{k} \tag{3}
$$

where κ is the thermal conduction coefficient of mixture, T is the temperature, and V_i and h_i are, respectively, the diffusion velocity and the specific enthalpy of species i.

The equations are completed by the equation of state and the constitutive relations for the coefficients of viscosity and conductivity. The equation of state is the ideal gas law with the specific heat ratio of 1.4 for air and 1.67 for helium.

Transport Properties

The transport properties in the mixing region are different from the individual pure gas. The molecular viscosity μ_i and conduction coefficients κ_i of the species i can be calculated by[15,16]

$$
\mu_i = 2.6693 \times 10^{-5} \frac{\sqrt{TM_i}}{d_i^2 \Omega_\mu} \tag{4}
$$

$$
\kappa_i = 1.9891 \times 10^{-4} \frac{\sqrt{T/M_i}}{d_i^2 \Omega_\kappa} \tag{5}
$$

where M_i, d_i are the molecular weight and the characteristic molecular diameter. The quantities Ω_μ and Ω_κ are collision integrals[15] which give the variation of the effective collision diameter as a function of temperature. The mixture values μ_m and κ_m are obtained from the values of μ_i and κ_i of each of the two species by means of Wilke's mixture rules. Then, the coefficients of viscosity μ and the thermal conductivity κ, which are used in system (1), can be written as,

$$\mu = \mu_m + \mu_t \tag{6}$$

$$\kappa = \frac{\gamma \mu_m}{Pr_m} + \frac{\gamma \mu_t}{Pr_t} \tag{7}$$

where Pr_m, denoting the molecular (laminar) Prandtl number, and Pr_t, denoting the turbulent Prandtl number are assumed to be constant ($Pr_m = 0.72$, $Pr_t = 0.9$). The turbulent eddy viscosity μ_t is calculated by applying a modified version of the Baldwin-Lomax model which is an algebraic turbulence model as proposed by Degani and Schiff[11]. For three-dimensional flow the calculation of high order models have been seldom used because of the inherent complexities and time-consuming computations. A simpler and more commonly used version of the Baldwin-Lomax model, which has been modified with consideration of the larger region of separation, is therefore chosen for the present study.

Boundary Conditions

The fluxes on the free boundaries, which are far enough from the interaction region and the induced separation zones, can be determined by using a characteristic relation based on Riemann invariants. The compatibility relations[17] associated with the acoustic waves can be written as,

$$R_n^{\pm} = V_n \pm \frac{2a}{\gamma - 1} \tag{8}$$

where $R_n^{\pm}$ is the Riemann variables and keep constant along the path $\vec{V} \pm a\vec{n}$, a is the speed of sound and $\vec{n}$ is a unit vector normal to the boundary surface. This treatment correctly accounts for wave propagation in the far field and avoids the reflection on the boundaries.

The solid wall boundary, except at the nozzle exit, is assumed to satisfy the no-flow-through condition and to be adiabatic. Therefore, the velocity at the solid wall must be set equal to zero, and there is no heat flux through the wall. Under experimental conditions, the jet flow properties might not be uniform at the exit of the converging nozzle. The ratio of mass flow rate to the ideal mass flow rate, the so-called the discharge coefficient, cannot reach unity, and it is decreased with decreasing P_{j0}/P_{∞}. In order to simulate the practical situation in the vicinity of the nozzle, the computational region was divided into an external block over the flat plate and an internal block for the nozzle, and the calculations were implemented by alternatively iterating block-by-block. The boundary fluxes on the interface of two blocks are evaluated from the results of the previous iteration for one block and then used as the interface fluxes for the other block. At the inlet boundary of an internal block, the total pressure ratio of jet-to-freestream and an inlet velocity are given to keep the mass flux equal to that at exit of sonic nozzle.

NUMERICAL ALGORITHM

According to the finite volume method, the governing equations could be directly discretized in the physical space. A system of ordinary differential equations is obtained by utilizing the spatial disretization separately in each cell. Therefore, the semi-discretized equations of any hexahedral cell of the structured grids can be written as follows,

$$\frac{\partial U}{\partial t} = -\frac{1}{\Delta \Omega} \sum_{k=1}^{6} (\Phi_k \Delta S_k), \tag{9}$$

where $\Delta \Omega$ is the volume of the cell, ΔS_k is the area of the kth surface of the cell, U contains the cell-averaged conservative variables and Φ_k is the fluxes through the surface. For the gas, dynamic simulation, the fluxes can be divided into the inviscid part, Φ_k^i, and the viscous part

(including heat fluxes), Φ_k^H; the inviscid part is evaluated by using Roe's flux function[18]. The inviscid flux through the kth surface of the cell reads

$$\Phi_k^i = \frac{1}{2} (\Phi_k^i (U_L) + \Phi_k^i (U_R)) - \frac{1}{2}|\hat{\Psi}|(U_R - U_L)$$

(10)

$$= \frac{1}{2} (\Phi_k^i (U_L) + \Phi_k^i (U_R)) - \frac{1}{2} R(\hat{U})|\hat{\Lambda}|R^{-1}(\hat{U})(U_R - U_L)$$

where U_R, U_L are the conservation variables at the immediate right and left hand side of the kth surface, respectively, and are evaluated by applying the high-resolution kappa scheme[19] (with a kappa number equal to 1/3). The Van Albada limiter was imposed in the kappa scheme to prevent numerical oscillation. $R(\hat{U})$ is the right matrix of the Jacobian matrix $|\hat{\Psi}|$. $|\hat{\Lambda}|$ is the eigenvalue matrix in which the characteristic speeds are $\hat{V} - \hat{a}$, $\hat{V}$, $\hat{V}$, $\hat{V}$, $\hat{V} + \hat{a}$ and $\hat{V}$, where $\hat{a}$ denotes the speed of sound at the kth surface. In this paper, the hats refer to the Roe (interface) averages; the Roe's average of density and a quantity A are evaluated as,

$$\hat{\rho} = \sqrt{\rho_L \rho_R}$$

and

$$\hat{A} = \frac{A_L \sqrt{\rho_L} + A_R \sqrt{\rho_R}}{\sqrt{\rho_L} + \sqrt{\rho_R}}, \text{ where } A = u, v, w, H^*$$

(11)

The other quantities with a circumflex, e.g. $\hat{a}$, are not averaged independently, but are obtained from the basic Roe-averaged quantities by their normal functional relation. The viscous fluxes are then calculated using a central differencing based on these Roe-averaged quantities.

In the original Roe's flux function, the artificial-viscosity matrix is based on the assumption of ideal gas with constant specific heat ratio. However, for air-helium mixture, the molecular mass M and the specific heat ratio γ are dependent on the air and helium mass fraction and are obtained as,

$$M = \frac{1}{\sum_i \frac{C_i}{M_i}}$$

(12)

$$\gamma = 1 + \frac{\sum_i \frac{C_i}{M_i}}{\sum_i \frac{C_i}{M_i(\gamma_i - 1)}}$$

(13)

Since the mixture-specific heat ratio is no longer a constant, the Roe's flux function has to be corrected for suiting the gaseous mixture. The right-eigenvector matrix $R(\hat{U})$ of the Jacobian matrix $|\hat{\Psi}|$ was re-derived as follows,

$$R(\hat{U}) = \begin{bmatrix} 1 & 0 & 0 & 1 & 1 & 0 \\ \hat{u} - \hat{a}\cos\alpha_\perp & \cos\alpha_{//,1} & \cos\alpha_{//,2} & \hat{u} & \hat{u} + \hat{a}\cos\alpha_\perp & 0 \\ \hat{v} - \hat{a}\cos\beta_\perp & \cos\beta_{//,1} & \cos\beta_{//,2} & \hat{v} & \hat{v} + \hat{a}\cos\beta_\perp & 0 \\ \hat{w} - \hat{a}\cos\gamma_\perp & \cos\gamma_{//,1} & \cos\gamma_{//,2} & \hat{w} & \hat{w} + \hat{a}\cos\gamma_\perp & 0 \\ \hat{H} - \hat{u}_\perp\hat{a} & \hat{u}_{//,1} & \hat{u}_{//,2} & \hat{V}^2\!\!\Big/_{\!2} & \hat{H} + \hat{u}_\perp\hat{a} & B \\ C_i & 0 & 0 & C_i & C_i & 1 \end{bmatrix}$$

(14)

where $\hat{V}$ is the velocity on the interface and $\hat{u}_\perp$, $\hat{u}_{//,1}$, $\hat{u}_{//,2}$ are the velocity components of $\hat{V}$ on the basis (e_1, e_2, e_3), as shown in *Figure 2*. We can find a set of basis on the kth surface; e_1 is a unit vector normal to the surface and e_2 and e_3 are unit vectors parallel to the interface. $cos\alpha_\perp$, $cos\beta_\perp$, ... etc. are the direction cosines of the basis. The correction term B can be written as,

$$B = \frac{\hat{\gamma}-1}{\hat{\gamma}} \bar{h}M \left(\frac{1}{(\gamma_{air}-1)M_{air}} - \frac{1}{(\gamma_{he}-1)M_{he}} \right) \qquad (15)$$

where M stands for molecular mass of the mixture and, the subscripts air and he denote the air and helium, and $\bar{h}$ is the specific enthalpy. The correction term is derived from the energy equation considering the change of the specific heat ratio while using $\frac{\gamma}{\gamma-1}\frac{p}{\rho}$ to replace the specific enthalpy. In addition, a simple version of Roe-averaged specific heat ratio at the kth surface, applied in the flux calculation can be chosen as,

$$\hat{\gamma} = \frac{\gamma_L + \gamma_R}{2} \qquad (16)$$

Equation (9) can be rewritten as,

$$\frac{\partial U}{\partial t} = \text{Res}(U) \qquad (17)$$

where $\text{Res}(U)$ is the sum of fluxes or the residual of the cell. After the residual for all cells in the computational region has been calculated, residual smoothing is performed implicitly to improve the damping and stability properties of the multi-stage scheme. The IRS[14] is applied in product form,

$$(1 - \varepsilon\delta_x^2)(1 - \varepsilon\delta_y^2)(1 - \varepsilon\delta_z^2) \text{Res}^{(av)}(U) = \text{Res}(U), \qquad (18)$$

i.e., approximate factorization is used to get the averaged residual, $\text{Res}^{(av)}(U)$. In (18), ε is the smoothing coefficient with the same value in three directions and δ_x^2, δ_y^2, δ_z^2 are the Laplace
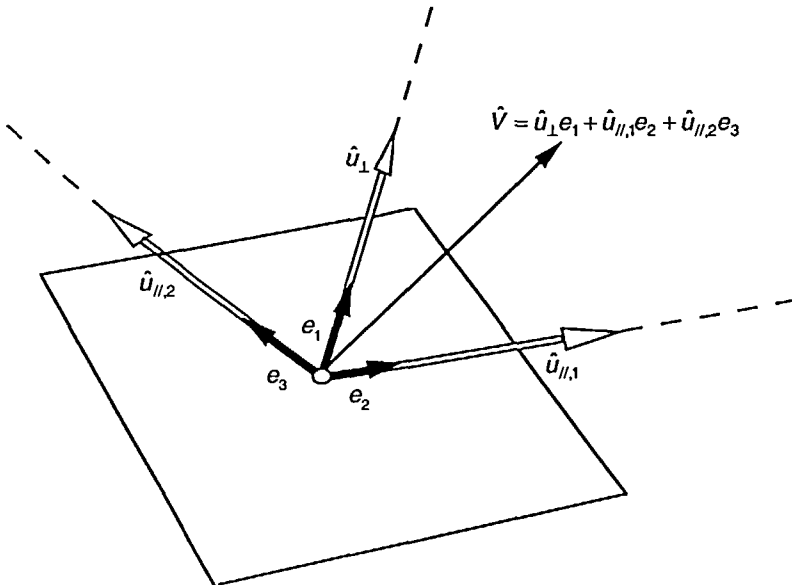

Figure 2   Geometry of any surface of cell for flux calculation

operators of central differencing. The optimally smoothing multi-stage scheme[12] is used for time integration,

$$U^{(0)} = U^n,$$

$$U^{(k)} = U^n - \alpha_k \Delta t \, \mathrm{Res}^{(av)}(U^{(k-1)}), k = 1, 2, ..., m; \alpha_m = 1 \qquad (19)$$

$$U^{n+1} = U^{(m)}.$$

The three-stage scheme with $\alpha_1 = 0.2883$, $\alpha_2 = 0.5009$, $\alpha_3 = 1$ is implemented and the IRS method with $\varepsilon = 0.4$ is applied in each stage in this study. The technique of local time-stepping, which allows each cell to advance in individual time at maximum rate, is also applied to speed up the convergence towards the steady state.

Computational grid

A two-dimensional structured grid is set up for the test calculations by applying an algebraic method. The grid is stretched near the wall and the nozzle exit, as shown in *Figure 3*. The multi-block grids strategy is adopted for the construction of the grid system, which includes calculated internal and external blocks. The external-large block is of rectangular shape using 128 × 64 grid points; and the internal-small block is of nozzle shape using 15 × 30 grid points. In our three-dimensional computations, three different shapes of nozzle exit are considered. The first one is a square shape of width 0.0105in. The computational grids in the external block are 96 grid points in the streamwise direction, 58 grid points in the direction normal to the flat plate, 40 points in the direction of the span and 15 × 30 × 15 grid points in the internal block. The second one is a rectangular shape of width 0.0315in and length 1in. The computational grids are 90 × 40 × 35 points in the external-large block and 27 × 24 × 18 grid points in the internal-small block. The last one is a circular shape of diameter 0.2in. and the area is the same as the rectangular one. The
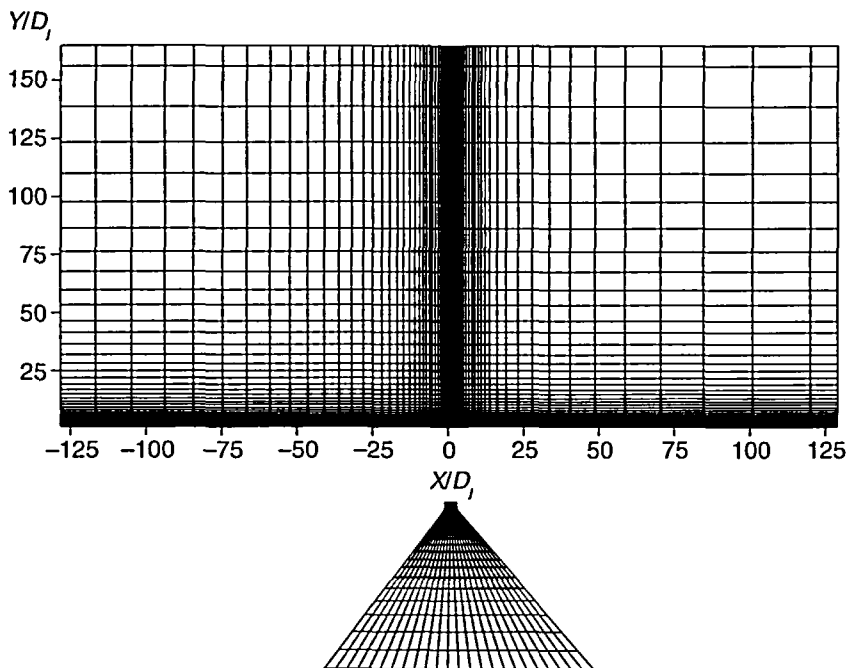

Figure 3 Computation grid for 2-D case

computational grids are $65 \times 45 \times 50$ points in the external block and $65 \times 30 \times 15$ grid points in the internal block. The computational grid systems constructed for the cases of rectangular jet and circular jet are shown in *Figure 4a* and *b*, respectively. The typical values of dimensionless normal distance y^+ for the grid points nearest to the wall are about 4~15, they are of the same order of the viscous sublayer thickness.

RESULTS AND DISCUSSION

The improved numerical solution procedure described above is implemented to calculate the interaction flowfield caused by sonic injection of gaseous helium in a cross-flowing, supersonic airstream. Two-dimensional test computations are performed first to simulate the flow conditions corresponding to the experiments of Spaid and Zukoski[7]. Three-dimensional computations are then carried out to investigate numerically the flow structures and mixing phenomena due to the interaction between the transverse rectangular, square, circular helium jets and the main airstream over a flat plate. All of the cases studied here adopted the same freestream conditions, which are Mach number $M_\infty = 2.61$, Reynolds number $Re = 2.6 \times 10^6$ per foot, total pressure $P_{\infty 0} = 19.4$psia, total temperature $T_{\infty 0} = 563°$R, and injection total pressure ratio $P_{j0}/P_{\infty 0} = 45.6$. All computations were performed on an HP-750 workstation and achieved a drop of residual to 5×10^{-6}. For the calculation using the $65 \times 45 \times 50$ grids, the CPU time of each iteration needed was about 25 seconds, and more than 15,000 iterations were necessary to reach the convergence criterion.

Comparison of computational and experimental results for two-dimensional test problem on static pressure distributions induced on flat plate surface by plane jet interaction is shown in *Figure 5*. The surface pressure upstream of the nozzle exit is seen to rise to a plateau and rise again to reach a peak immediately near the jet. The extent of the pressure plateau and value of the pressure peak are slightly overpredicted by the present numerical method. The predicted static
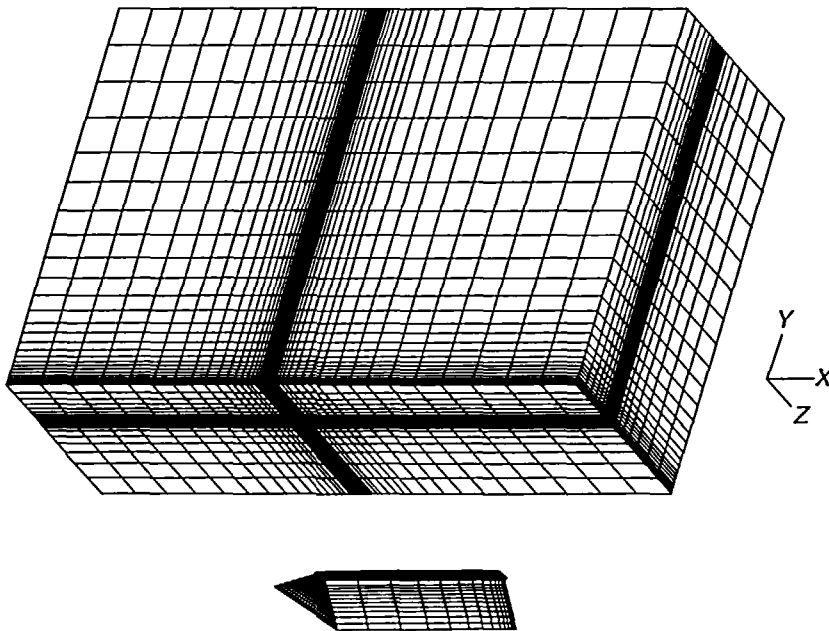

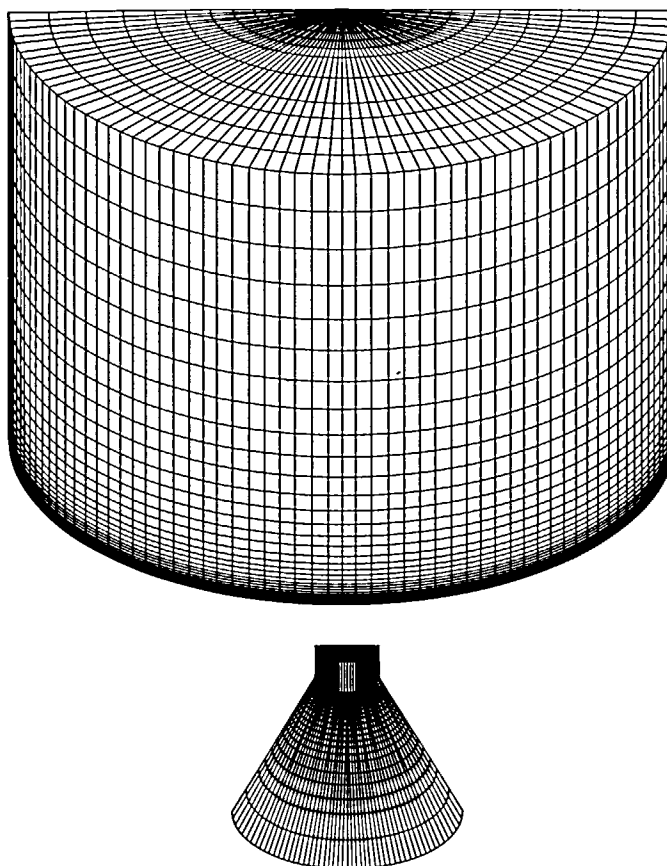*Figure 4a*   Computation grid for 3-D case – rectangular jet

Figure 4b Computation grid for 3-D case – circular jet

pressure distribution downstream of the jet is much closer to that of the experimental data. Considering the experimental uncertainty in measurements in the near jet region, the overall agreement is quite satisfactory. Some of the discrepancies between the numerical solution and the experimental data may be, to some extent, due to the presence of unsteady features, the inadequacies of the turbulence model and coarseness of the grid system used. A convergence comparison of the three-stage scheme, with and without IRS, is shown in *Figure 6*. Maximum allowable Courant numbers were adopted to keep the computation stable. It is seen that the use of IRS can speed up the convergence effectively, because of the better damping properties and the larger Courant number.

Figure 7 shows the corresponding surface pressure distributions for two cases of three-dimensional computations. *Figure 7(a)* represents the results on surfaces at the symmetry plane and four side positions for the case of a square jet. A bow-shock-like structure is evident as shown by downstream shifting of pressure peaks. *Figure 7(b)* represents the results on surfaces at five spanwise locations in a rectangular jet. It is revealed that the pressure peak and the extent of the upstream and downstream interaction regions decrease gradually as the sideward distance of the x-y plane from the symmetrical plane ($z = 0$) increases. This is attributed to the weakening influence of the interaction between the jet and crossflow in the z-direction.

A good insight into the flow development in the near field of jet injection can be gained by constructing the plots of particle traces. For steady flow, particle traces are equivalent to
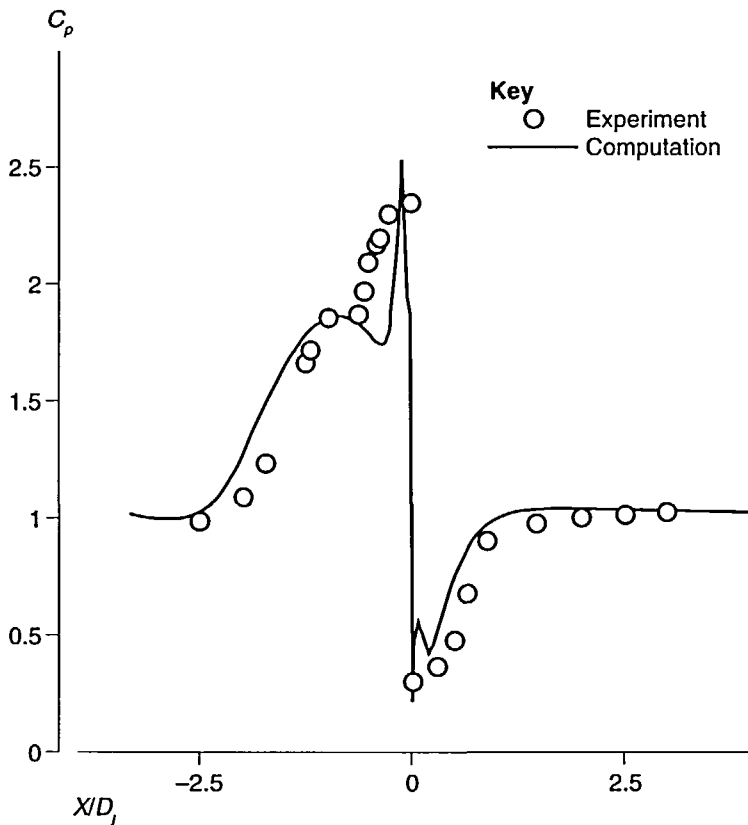
Figure 5   Surface static pressure distributions for 2-D case

streamlines and can be computed by releasing particles that move with local flow velocities originating from selected spatial locations. *Figures 8(a)*, (*b*), (*c*) show three-dimensional streamlines of the flow field for a rectangular jet, square jet and circular jet injections, respectively. These illustrate how the jet and cross flow interact with each other. The mutual deflection of the two flows can be clearly seen in all three figures. In *Figure 8*(a), for the case of a rectangular jet with a slot aspect ratio 31.4, it shows the presence of upstream and downstream separated flow regions near the symmetry plane. This is similar to that of the case of a two-dimensional transverse jet. Three-dimensional effects appear where mainstream fluid tends to flow from sides towards the centre plane which travel upstream, move upward and finally flow downstream.

For the cases of square jet and circular jet as shown in *Figure 8(b)* and (*c*), a similar primary vortex pattern and its downstream development are observed. This is different from that for rectangular jet because the main air can flow and mix easily underneath the square (or circular) jet and generates a vortex flow motion. The velocity gradient near the interface of the jet and the crossflow is steep. Vortices along the jet direction and vortex sheet around the jet are developed, roll up and deflect into the streamwise direction. Secondary vortices, beneath the primary vortex, are also observed to form very near the plane wall. These primary and secondary vortices may affect wake growth, jet entrainment and turbulent mixing of the flowfield and, therefore, are of interest to investigators. *Figures 9(a)*, (*b*), and (*c*) display this important vortex flow pattern in velocity vector plots on the planes of $X/D_j = 4.1, 27, 41$ downstream of the square jet. The upward
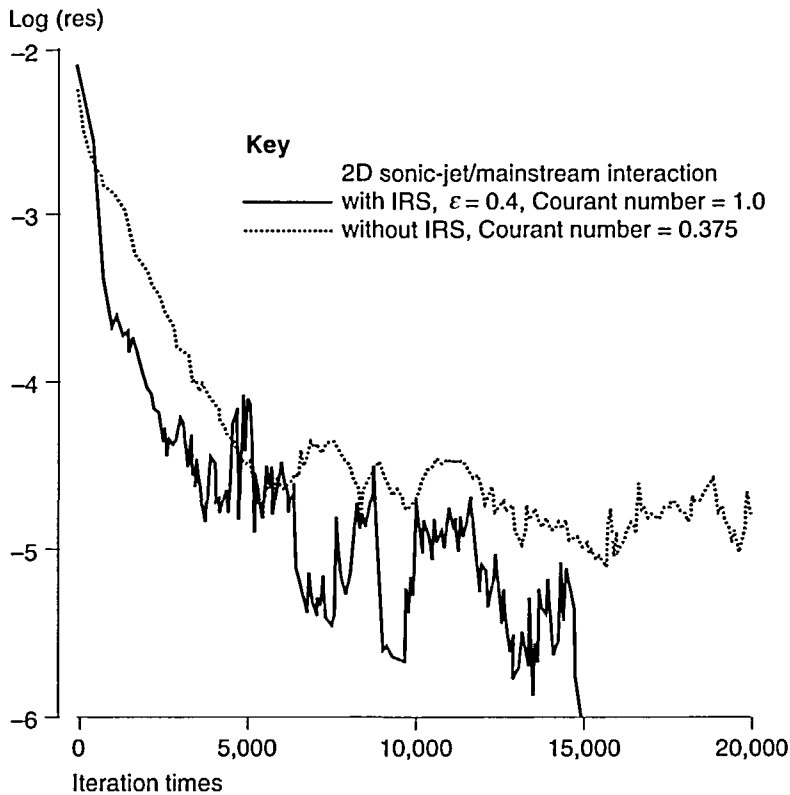
Figure 6 Convergence history of three-stage scheme with and without IRS

displacement of the primary vortex is clearly shown. The enlarged diagram in *Figure 9*(b) also shows the small secondary vortex.

Figure 10 shows the plots of Mach number contours on planes of constant *y* at two positions upward of the circular jet orifice. *Figure 11* displays the distribution contours of helium mass fraction on the same two planes. The noteworthy features seen in these figures are the evolution of jet cross-sections from circular to the characteristic kidney-like shape and the presence of a reverse flow region just downstream of the jet orifice and a wake-like region thereafter. These are in qualitative agreement with the available experimental data[20,21]. The contour plots of helium mass fraction on planes of constant *z* at various locations sideward of the rectangular jet and square jet are shown, respectively, in *Figures 12* and *13*. These also provide an insight into the general features of the flow. The helium jet penetration for the case of square exit is observed to be approximately twice as high (as seen by helium fraction contour lines of 8%) than that for a rectangular exit. Beginning at the injection nozzle, tongue-like contours can be seen that turn downstream. Notice that, for a rectangular jet, helium is diffused along the wall well upstream of, the jet. This is due to the flow recirculation ahead of the jet. Comparing it with a square jet, it is also observed that the rectangular helium jet and air flow are not well mixed, a helium rich region along the wall extends well downstream. The three-dimensional effect on mixing is evident near the side edge of both jets.

In addition, one can observe that the influence of the grid coarseness plays an important role in the diffusion of the helium jet. As shown in *Figures 10* and *11*, the bow shock at the surface $Y/D_j = 2.1$ is sharper and less diffused than that at the surface $Y/D_j = 0.185$. This is somehow because
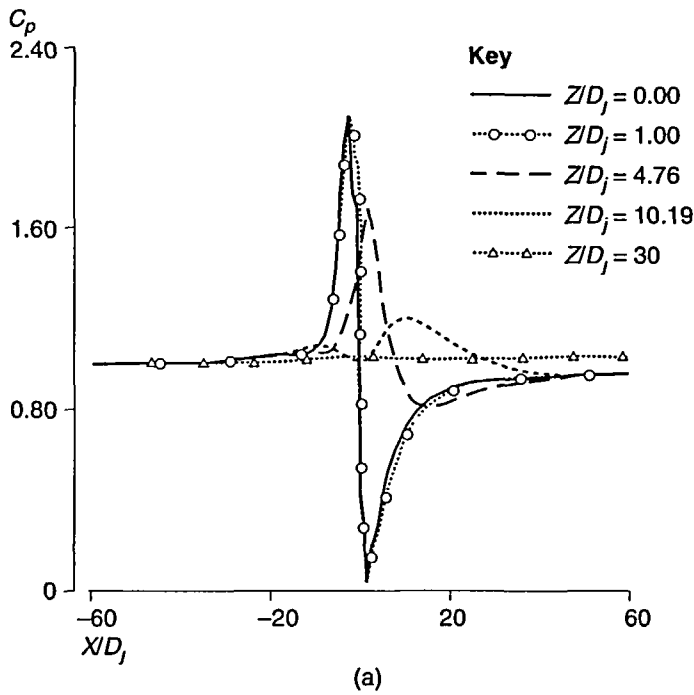
Figure 7a   Surface static pressure distributions for 3-D case – square jet
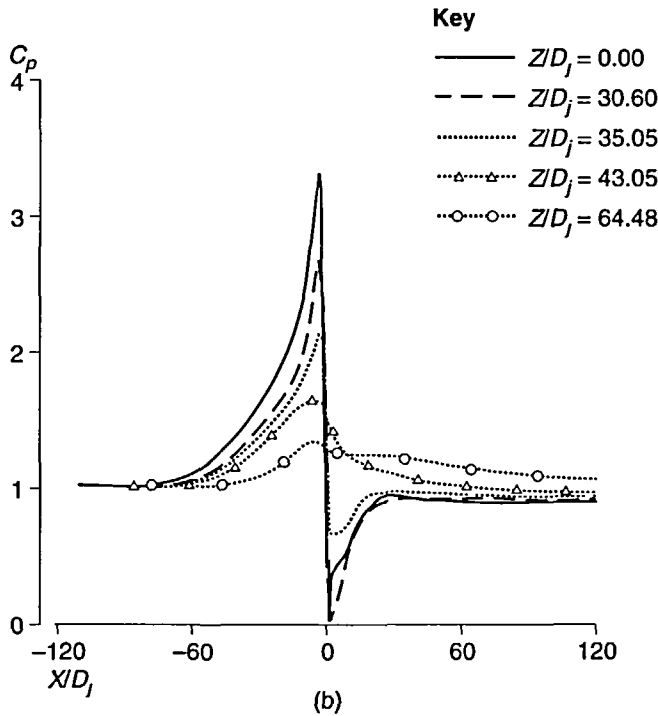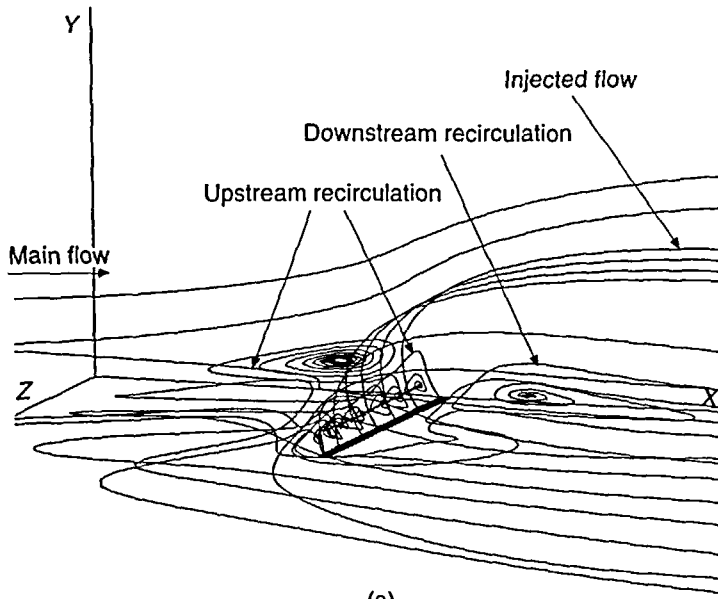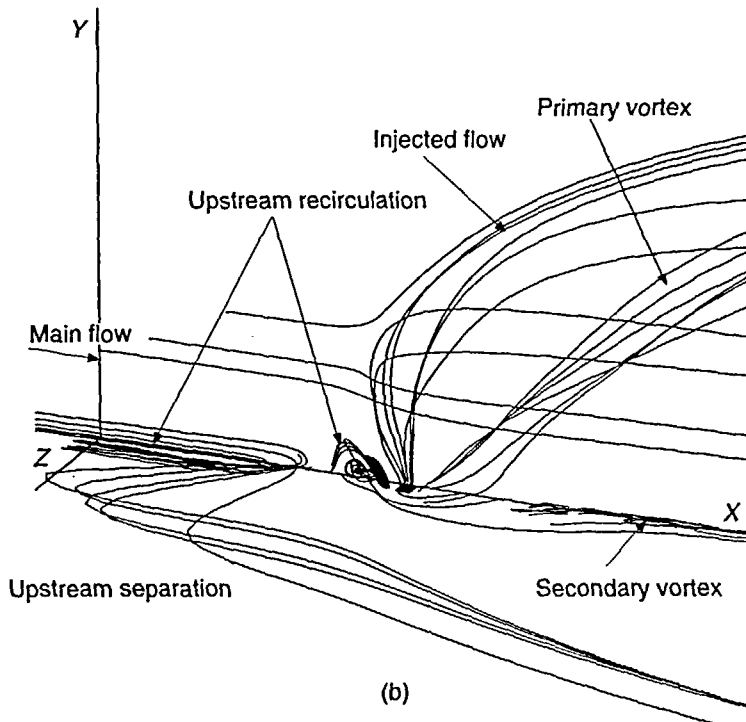

Figure 7b   Surface static pressure distributions for 3-D case – rectangular jet

(a)

Figure 8a The streamline diagram – regtangular jet

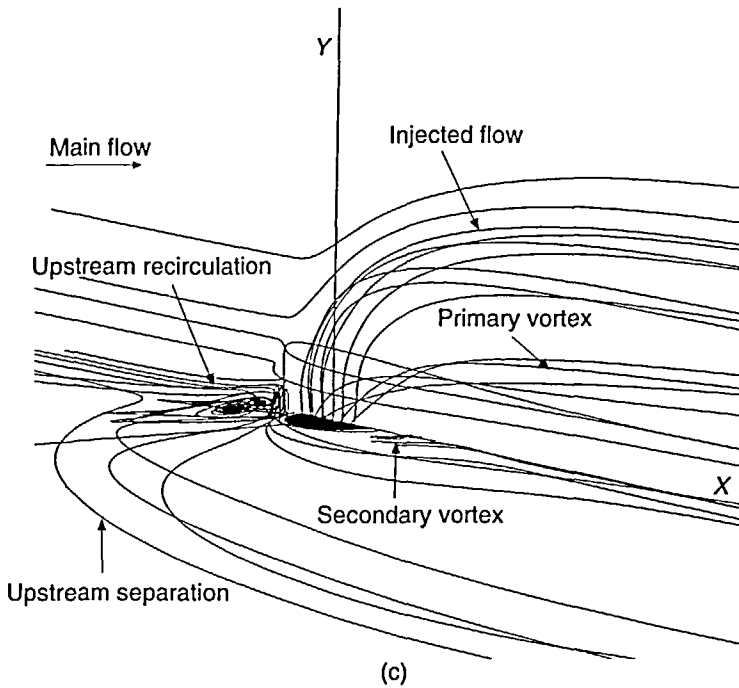
(b)

Figure 8b The streamline diagram – square jet

Figure 8c   The streamline diagram – circular jet

at larger Y/D_j the bow shock occurs closer to the y-axis where the grid lines are clustered. Similar situations can be observed for the results shown in *Figures 12* and *13*. Therefore, the diffusion of helium jet may also depend on the relative coarseness of the grid. The limitation imposed by computer time and storage prohibits the use of very fine grids in three-dimensional computations. In this study, the maximum available grid with similar coarseness and distribution has been employed for each case. More accurate solutions will certainly be obtained with further refined grids in the future.

The three-dimensional Mach number contours for the square and rectangular shape of the nozzle exit are presented in *Figure 14(a)* and *(b)*. The selected planes are the symmetrical plane, the near wall plane and a plane of constant x downstream of the jet orifice. According to the clustering of the contour lines, it is shown that the strength of a shock system on the symmetrical plane in front of the jet, for a square exit case, is stronger than that of the rectangular exit case. This can also be inferred by comparing the pressure rise between *Figures 7(a)* and *7(b)*. The upstream separation, induced shock, Mach disk and the associated jet structure are also shown. The three-dimensional mass fraction profiles of injected helium are presented in *Figure 15(a)* and *(b)*. The entire configuration of injected jet can be clearly seen, and it is found that the concentration of helium upstream of the rectangular exit is higher than that for the square exit case. This is due to the stronger blockage effect which enhances the upstream mass diffusion. After comparing the results of three exit shapes, it appears that, for better mixing in combustion application, square and circular exits are more desirable than rectangular ones, while for inducing force and moment in reaction control application, a rectangular exit may be preferable in some circumstances.
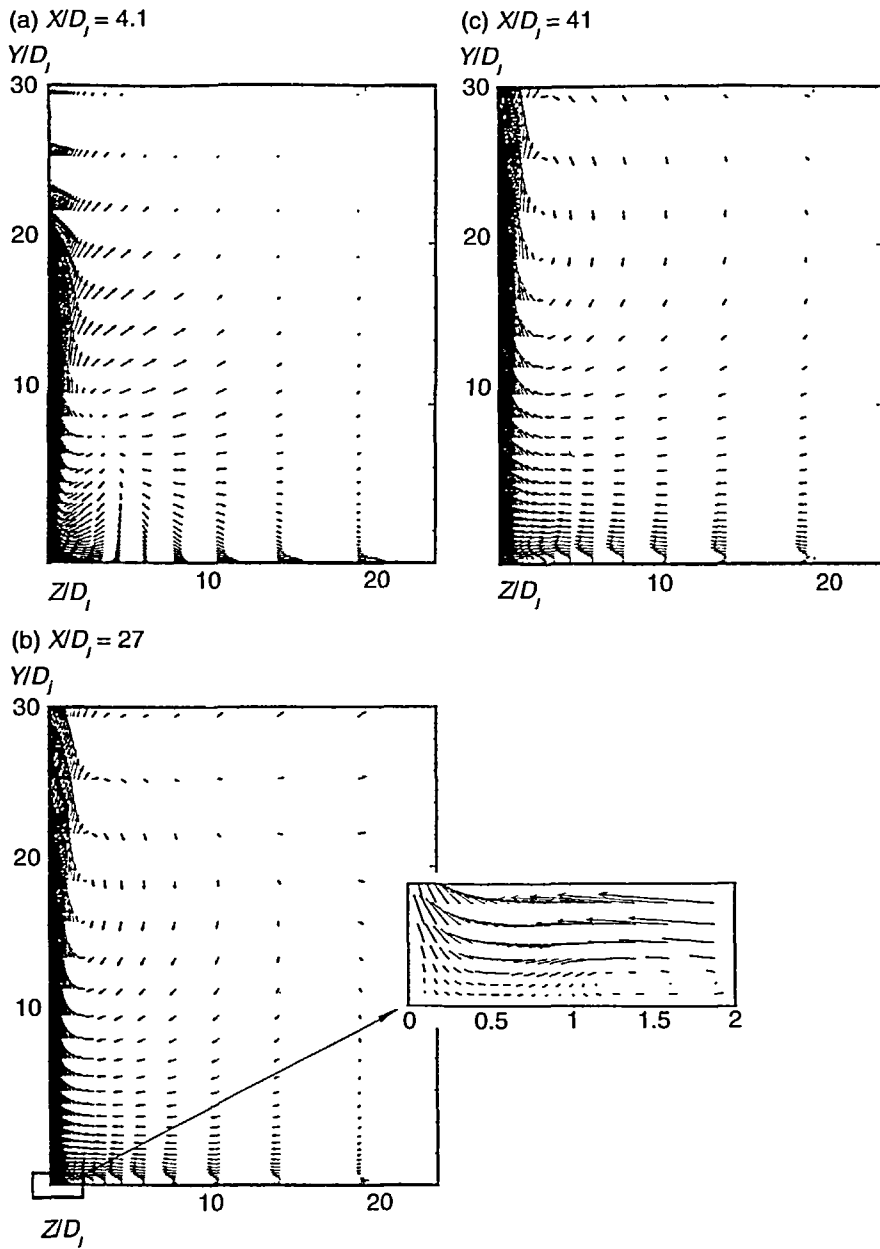
Figure 9   Velocity vector plots on the y-z plane (a) X/D_j = 4.1 (b) X/D_j = 27 (c) X/D_j = 41
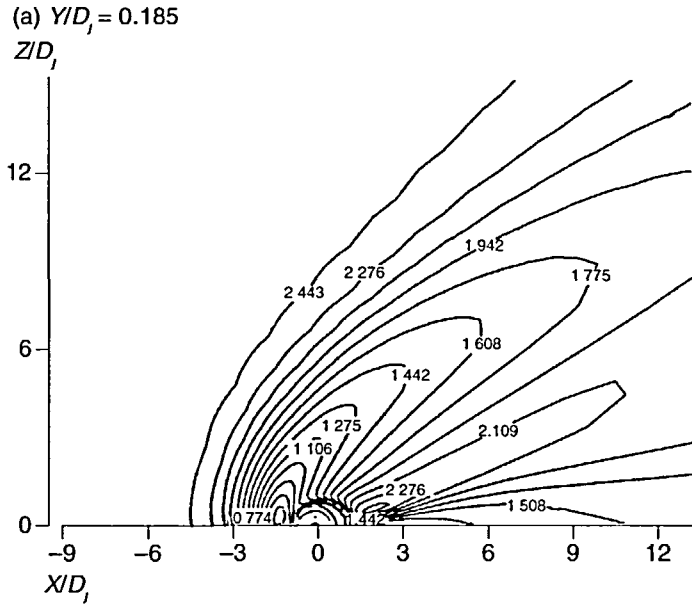
(a) $Y/D_j = 0.185$

Z/D_j

Figure 10a   Mach contours on the x-y planes for the circular jet – $Y/D_j = 0.185$

(b) $Y/D_j = 2.1$

Z/D_j
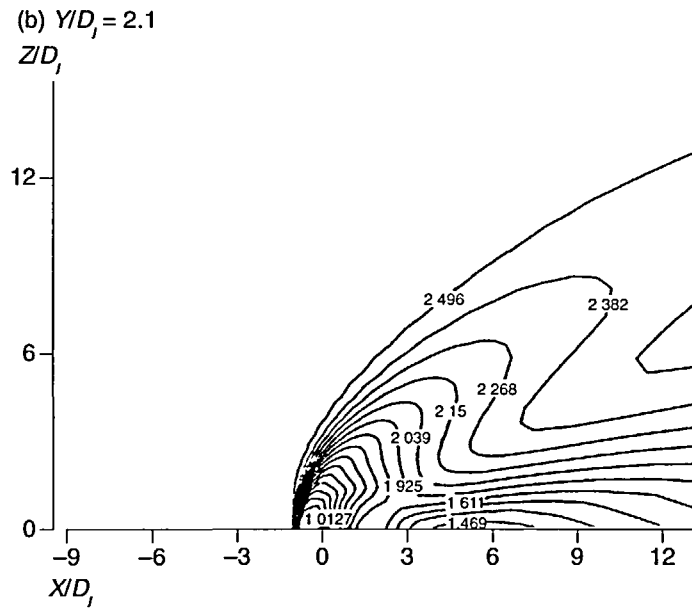
Figure 10b   Mach contours on the x-y planes for the circular jet – $Y/D_j = 2.1$

(a) $Y/D_j = 0.185$

Z/D_j

0 117

0 117

0 145

0 174

0 202

0 032

0 0607

0 089

X/D_j
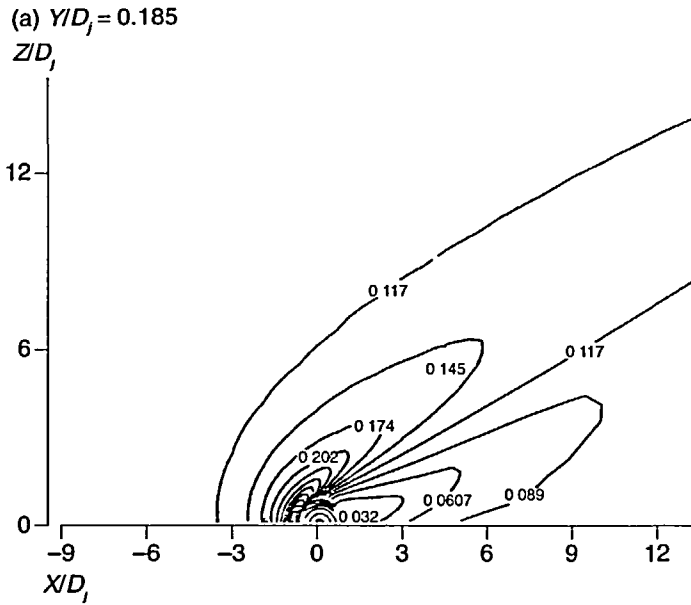
Figure 11a Contours of helium mass fraction on the x-y planes for the circular jet – $Y/D_j = 0.185$

(b) $Y/D_j = 2.1$

Z/D_j

0 1456

0 187

0 229

0 103

0 103

0 693

X/D_j
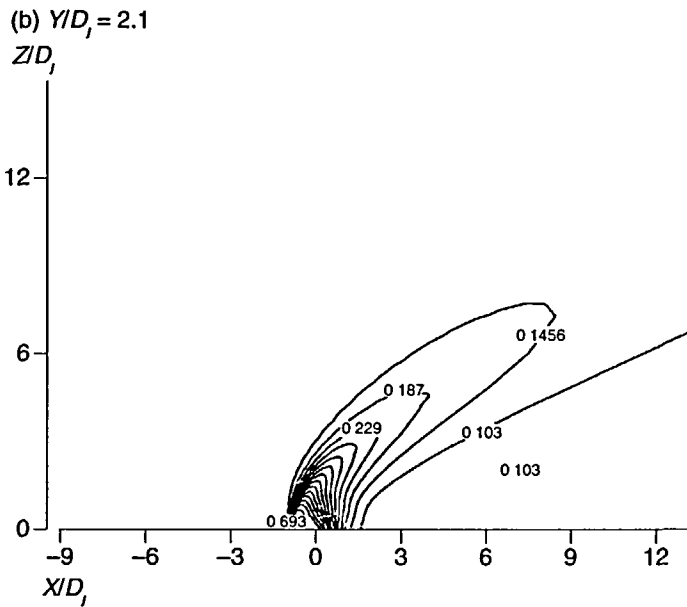
Figure 11b Contours of helium mass fraction on the x-y planes for the circular jet – $Y/D_j = 2.1$
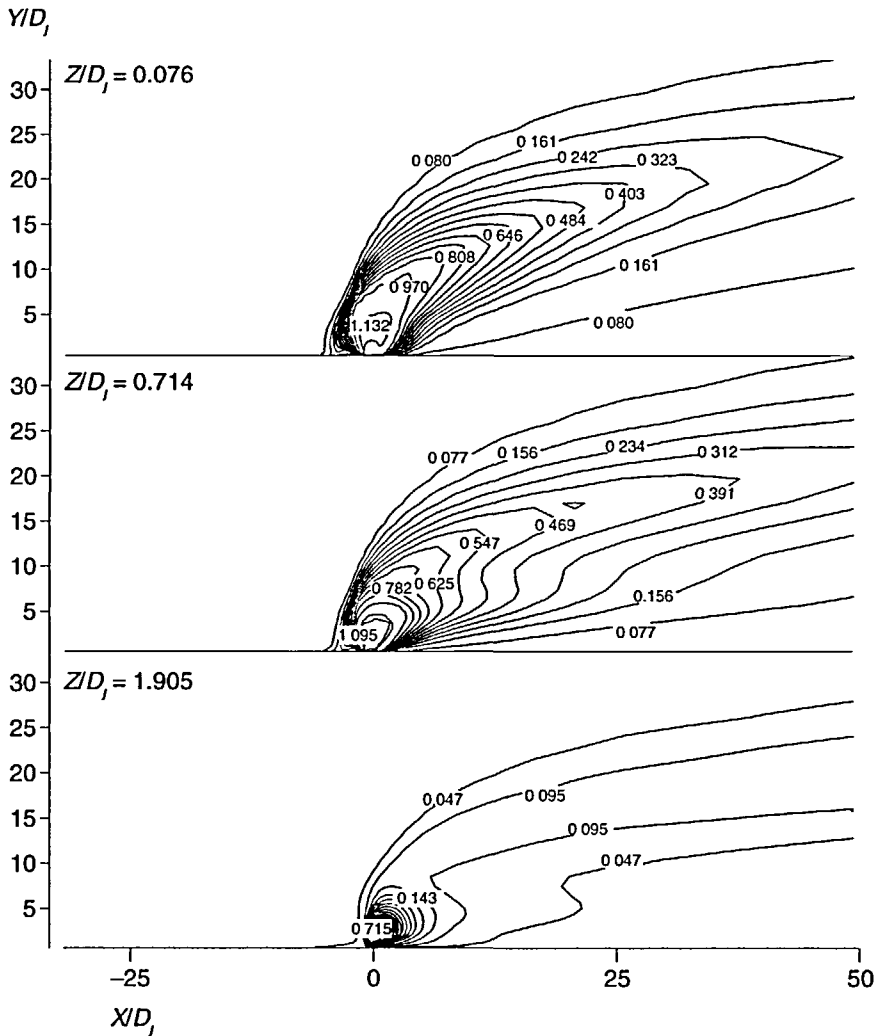
Figure 12   Contours of helium mass fraction on the *x-y* planes for the square jet

CONCLUSIONS

A numerical study of the gas-dynamic interaction between transverse helium jet and a supersonic airflow has been performed. The main conclusions which can be drawn are as follows:

1 An efficient finite-volume method is employed. Convergence acceleration techniques, such as local time stepping and implicit residual smoothing, are successfully implemented to facilitate the three-dimensional computations. The upwind relaxation algorithm, the modified Roe's function and multi-block grid strategy appear to perform reasonably well for the present application.

2 Flow patterns which emerge from the calculated results demonstrate that all of the essential characteristics of the flowfield associated with transverse jets in a supersonic main stream are well predicted. Although for the three-dimensional cases there is a lack of adequate
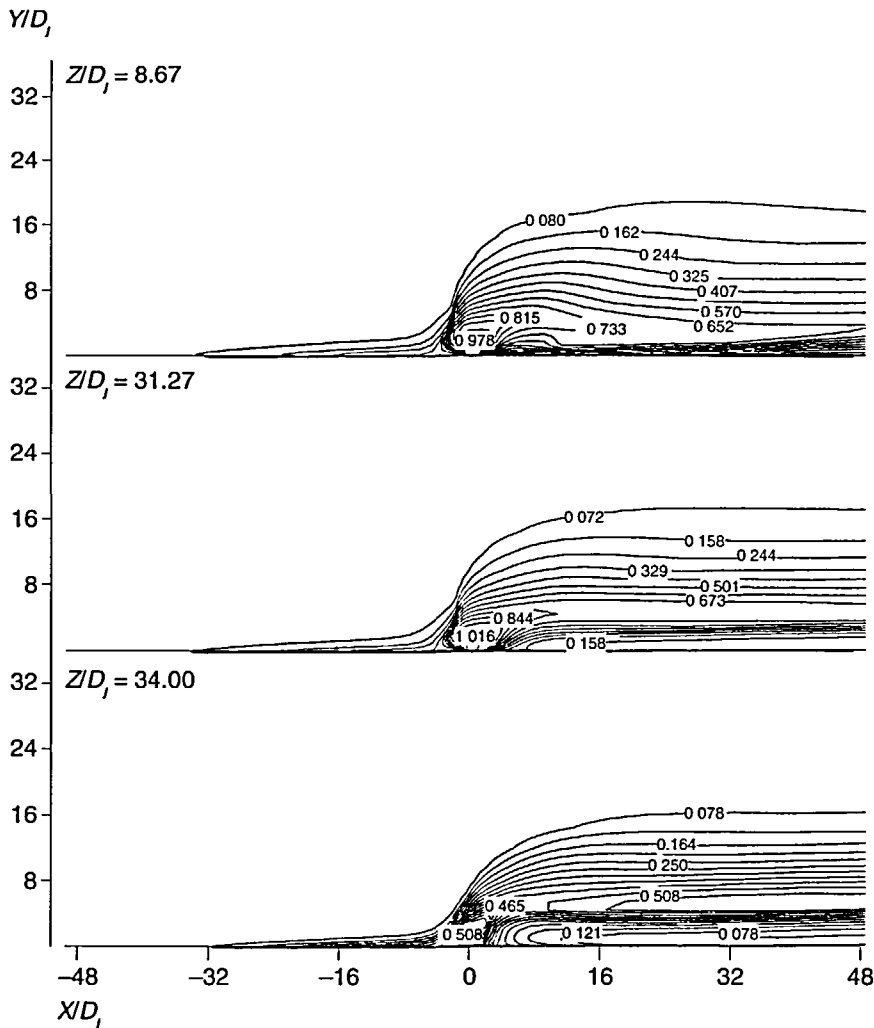
Figure 13 Contours of helium mass fraction on the *x-y* planes for the rectangular jet

experimental data to verify the accuracy quantitatively, the numerical solutions can still be very valuable in providing insight into this complicated flow situation.

3 The effects of different shapes of nozzle exit are observed. In general, the square and circular exits may result in better helium-air mixing than the rectangular exit of high slot aspect ratio. The rectangular transverse jets may, however, produce a more desirable surface pressure distribution in some reaction control applications.

REFERENCES

1 Werle, W.J. *A Critical Review of Analytic Method for Estimating Control Forces Produced by Secondary Injection —The Two-dimensional Problem*, NOL TR 68-5 (AD 669445) (1968)
2 Spaid, F.W. and Cassel, L.A. *Aerodynamic Interference Induced by Reaction Controls*, AGARD-AG-173 (AD-775209) (1973)
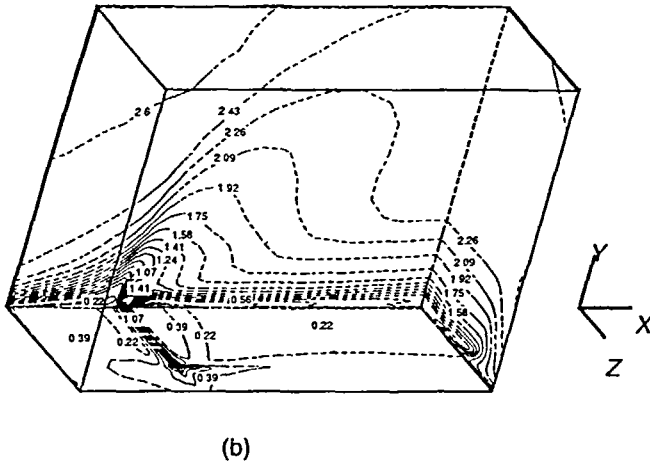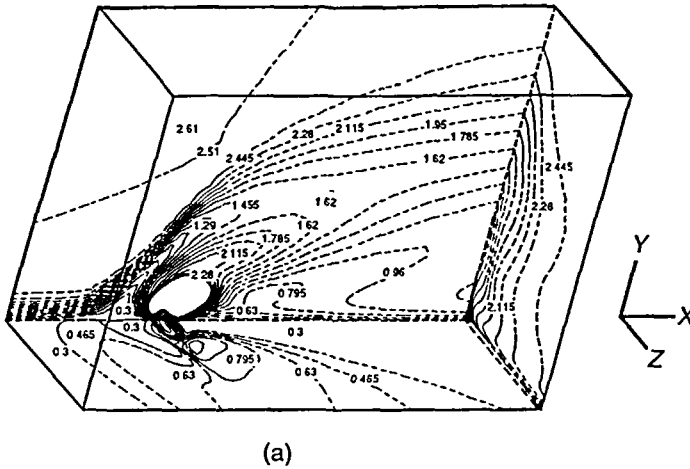
(a)

(b)

Figure 14   Three-dimensional Mach number profiles near the jet orifice (a) square jet (b) rectangular jet

3   Aso, S., Okuyama, S. and Kawai, M. Experimental study on mixing phenomena in supersonic flows with slot injection, *AIAA paper 91-0016* (1991)

4   Harloff, G.J. and Lytle, J.K. Three-Dimensional Viscous Flow Computations of a Circular Jet in Subsonic and Supersonic Cross Flow, *AIAA paper 88-3703* (1988)

5   Cubbison, R.W., Anderson, B.H. and Ward, J.J. *Surface Pressure Distributions with a Sonic Jet Normal to Adjacent Flat Surfaces at Mach 2.92 to 6.4*, NASA TN D-580 (1961)

6   Thompson, D.S. Numerical solution of a two-dimensional jet in a supersonic crossflow using an upwind relaxation scheme, *AIAA Paper 89-1869* (1989)

7   Spaid, F.W. and Zukoski, E.E. A study of the interaction of gaseous jets from transverse slots with supersonic external flows, *AIAA J.*, 5, 882-884 (1967)

8   Dormieux, M., Guillen, P. and Abgrall, R. Numerical simulation of transverse jet flows by a non reactive two apecies multidomain Euler flow solver, *AIAA Paper 90-0126* (1990)
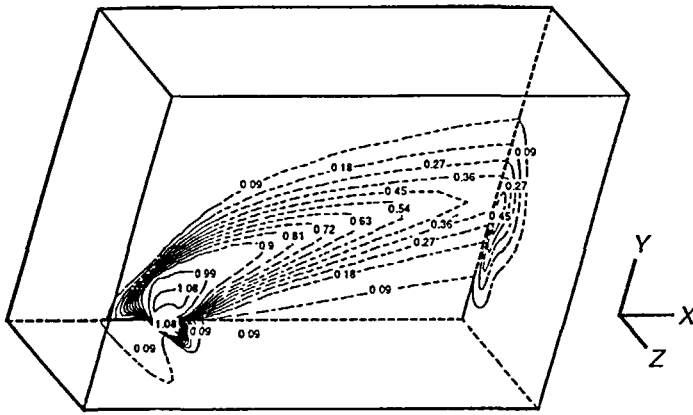
(a)
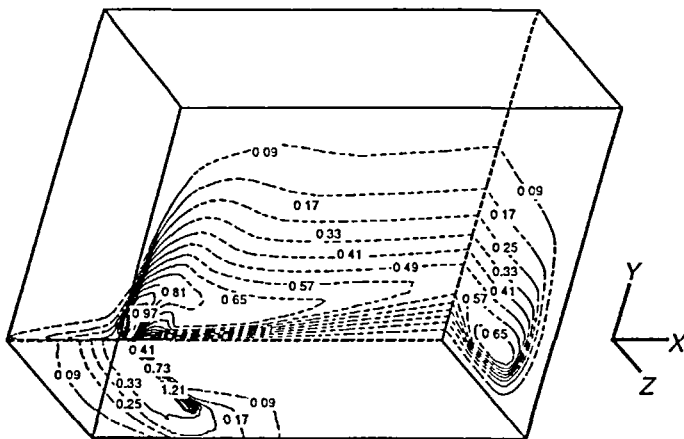
(b)

Figure 15   Three-dimensional profiles of injected helium mass fractions near the jet orifice
(a) square jet (b) rectangular jet

9   Takahashi, M. and Hayashi, A.K. Numerical study on mixing and combustion of injecting hydrogen jet in a supersonic air flow, *AIAA Paper 91-0574* (1991)

10   Rizzetta, D.P. Numerical simulation of slot injection into a turbulent supersonic stream, *AIAA J.*, **30**, 10, 2434-243 (1992)

11   Degani, D. and Schiff, L.B. Computation of supersonic viscous flows around pointed bodies at large incidence, *AIAA paper 83-0034* (1983)

12   Tai, C.H, Sheu, J.H. and van Leer, B. Optimal multistage scheme for Euler equations with residual smoothing, *AIAA J.*, **33**, 6, 1008-1016 (1995)

13   Jameson, A. Numerical solution of the Euler equations for compressible inviscid fluids, *Num. Meth. for the Euler Equations of Fluid Dynamics*, Angrand, F., Dervieux, A., Desideri, J.A. and Glowinski, R. (Eds), SIAM, Philadelphia, 199-245 (1985)

14 Hirsch, C. *Numerical Computation of Internal and External Flow*, 1st ed., Vol. 2, John Wiley & Sons Ltd, New York, Chapter 1 (1988)
15 Anderson, J.D. *Hypersonic and High Temperature Gas Dynamics*, McGraw-Hill Book Company, N.Y., Chap. 18-19 (1989)
16 Bird, R.B., Stewart, W.E. and Lightfoot, E.N. *Transport Phenomena*, John Wiley and Sons, New York, Ch. 3-4 (1960)
17 Thomas, J.L. and Salas, M.D. Far field boundary conditions for transonic lifting solutions to the Euler equations, *AIAA J.*, **24**, 1074-1080 (1986)
18 Roe, P.L. Approximate Riemann solvers, parameter vector, and difference schemes, *J. Comput. Physics*, **43**, 357-372 (1981)
19 van Leer, B. Upwind-Difference Methods for Aerodynamic Problems Governed by the Euler Equations, in Large-Scale Computations in Fluid Mechanics, *Lectures in Applied Mathematics*, **22**, 327-336 (1985)
20 Moussa, Z.M., Trischka, J.W. and Eskinazi, S. The Near Field in the Mixing of Round Jet with a Cross-stream, *J. Fluid Mechanics*, **80**, 49-80 (1977)
21 Andreopoulos, J. and Rodi, W. Experimental Investigation of Jets in a Crossflow, *J. Fluid Mechanics*, **138**, pp.93-128 (1984)